

BEAD-PULL MEASUREMENTS OF THE MAIN DEFLECTING MODE OF THE DOUBLE-QUARTER-WAVE CAVITY FOR THE HL-LHC *

M. Navarro-Tapia[†], R. Calaga, CERN, Geneva, Switzerland

Abstract

A full-scale model of the double-quarter-wave (DQW) cavity towards the High-Luminosity Large Hadron Collider (HL-LHC) upgrade was built in aluminum to characterize the deflecting mode. Field strength measurements have been carried out for both the transverse and longitudinal electromagnetic fields, by using the bead-pull technique. A reasonably good agreement was found between numerical simulation and measurements, which confirm the reliability and accuracy of the measurements done.

INTRODUCTION

The novel machine configuration of the LHC, called High-Luminosity LHC (HL-LHC) [1], will rely on a number of innovative technologies, such as the use of superconducting deflecting cavities for beam rotation (crab cavities). These cavities are designed to deflect/crab the beam at 400 MHz [2], where the transverse kick results from the interaction of the particle with both the transverse electric and magnetic fields. The double-quarter-wave (DQW) cavity [3] is one of the candidates to be considered.

In order to assess the manufacturing process and validate the tolerances after fabrication, comprehensive radio-frequency (RF) measurements will be needed. This article reports the first RF tests that have been carried out on a full-scale aluminum prototype of the DQW cavity. The RF characterization of the fundamental deflecting mode, for both the transverse and longitudinal electromagnetic fields, has been done by means of bead-pull measurements.

PROTOTYPE DESCRIPTION

Geometry

Figure 1 is a schematic showing the cavity geometry, which can be seen as a double $\lambda/4$ line with symmetric poles –also referred to as “domes”– to create a transverse electric field and cancel any longitudinal field. The deflection in this case is mainly due to the strong transverse electric field between these parallel domes. The aperture of the domes is equal to the diameter of the incoming and outgoing beam pipes ($\varnothing 42$ mm).

Figure 1 also shows the definition of the reference coordinate system that will be used in this paper. The beam-pipe axis is oriented along the \hat{z} -direction, so that the kick takes place in the \hat{x} -direction, following the orientation of the electric field lines there.

* The research leading to these results has received funding from the European Commission under the FP7 project HiLumi LHC (Grant agreement no. 284404), and under a Marie Curie action (Grant agreement PCOFUND-GA-2010-267194).

[†] maria.navarro-tapia@cern.ch

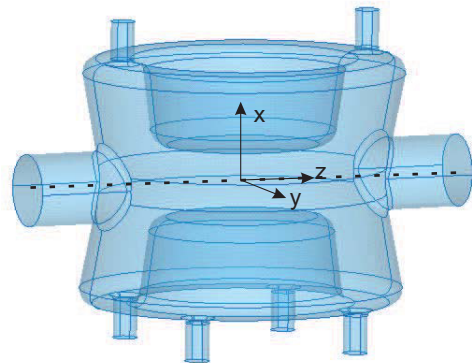


Figure 1: Schematic of the DQW cavity geometry and coordinate system definition.

The first higher-order mode is resonating at ~ 578 MHz, around 180 MHz apart from the fundamental mode. This mode only has a longitudinal component of the electric field on axis, which will be useful when calibrating the longitudinal form factor of any needle-like perturbing object.

A full-scale prototype of the DQW cavity –made out of aluminum– has been built at CERN to carry out the first RF measurements. Figure 2 shows a picture of the prototype, with the beam-pipe axis lying vertically. The drawings with the exact dimensions of this prototype can be found in [4].

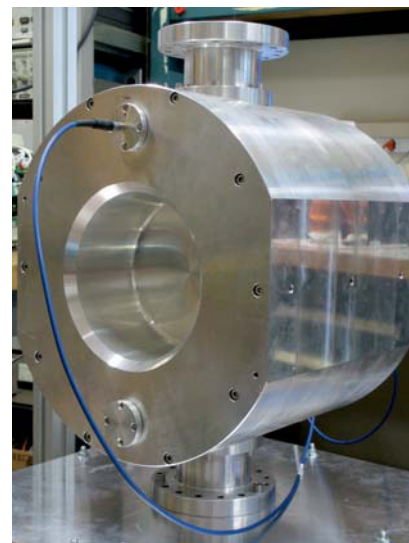


Figure 2: Full-scale aluminum prototype of the DQW cavity. The beam-pipe axis is lying vertically.

Deflecting-Mode Field Distribution

In order to analyze the field configuration of the fundamental deflecting mode of the DQW cavity at ~400 MHz, electromagnetic full-wave simulations have been carried out by means of HFSS [5], a commercial finite-element-method solver.

A detailed look into the field profile is done by extracting the different field components along the cavity axis. Figure 3 collects both the on-axis and the off-axis field magnitude of the different components of the electric field, $|E_n|$, and the magnetic field, $|H_n|$, where n denotes the corresponding coordinate (x , y or z). The magnetic field is represented multiplied by the free-space impedance, $\eta_0 \approx 120\pi$, in order to establish a fair comparison of the respective contribution of the electric and magnetic fields to the transverse kick. Note that all the components are normalized to the square root of the stored energy, \sqrt{U} .

The field components present on the cavity axis (on axis) are the transverse E_x and H_y , both responsible of the particle kick. It can be observed that the main contribution to the kick is coming from the transverse electric field. In Fig. 3, these components are also represented at 9 mm and 18 mm

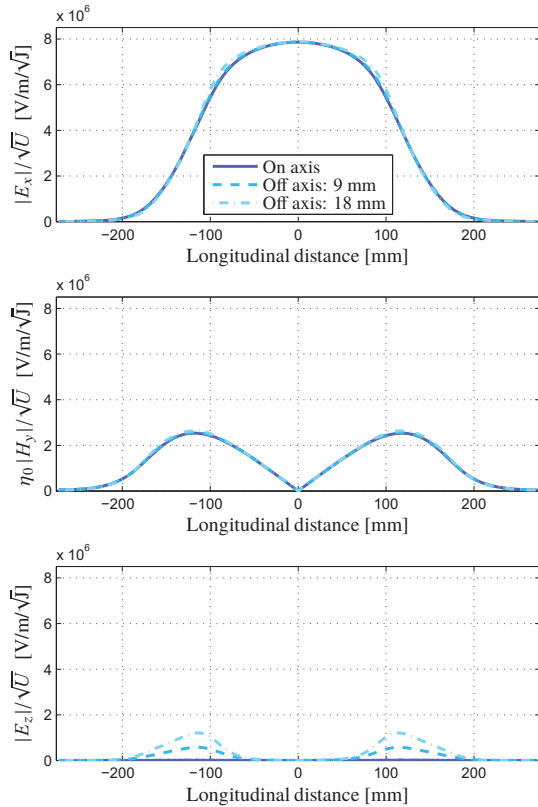


Figure 3: Simulated magnitude of the field components along different lines lying **on-axis** and **off-axis in the \hat{x} direction**. Both electric and magnetic fields are normalized to the square root of the stored energy.

off-axis in the \hat{x} direction. It is clear that these transverse fields have little variation across the cavity aperture. This fact will be important to take into account when characterizing the longitudinal fields with bead-pull measurements.

However, as going off axis, a new contribution of the longitudinal electric field component, E_z , starts to get noticeable in Fig. 3. The presence of these longitudinal components off-axis is something expected from the Panofsky-Wenzel theorem [6], stating that the transverse kick that a particle undergoes is due to the transverse inhomogeneity of the longitudinal electric field. It can be seen that the strength of E_z is much lower than that of the transverse fields, around 6 times lower than $|E_x|$ at 18 mm.

SMALL-PERTURBATION THEOREM

An experimental method to measure the field distribution in a resonant electromagnetic cavity was already proposed by Slater in 1950 [7–9]. This method relies on the fact that the perturbation of the cavity volume by a small amount will cause an unbalance of the electric and magnetic stored energies and, therefore, the resonant frequency of the cavity will shift to restore this unbalance. If the perturbation is small enough, this frequency shift is proportional to the original amount of energy stored in the perturbing object. Being the stored energy proportional to the square of the electromagnetic fields, $|\vec{E}|^2$ or $|\vec{H}|^2$, the shift in resonant frequency will depend on the local electric and magnetic fields at the position of the perturbing object. Therefore, this theorem offers a way to measure the fields in the cavity, just by measuring the change in resonance frequency when causing a small perturbation in the cavity. Under this assumption of small perturbation, the frequency shift of the cavity resonance is given by:

$$\frac{\Delta\omega}{\omega_0} = \alpha_{E_{\perp}} \varepsilon_0 \frac{|E_{\perp}|^2}{U} + \alpha_{E_{\parallel}} \varepsilon_0 \frac{|E_{\parallel}|^2}{U} + \alpha_{H_{\perp}} \mu_0 \frac{|H_{\perp}|^2}{U} + \alpha_{H_{\parallel}} \varepsilon_0 \frac{|H_{\parallel}|^2}{U}, \quad (1)$$

where ε_0 and μ_0 are the vacuum permittivity and permeability, respectively; and E_{\perp} , E_{\parallel} , H_{\perp} and H_{\parallel} are the electric and magnetic fields perpendicular and parallel to the perturbing object. The coefficients $\alpha_{E_{\perp}}$, $\alpha_{E_{\parallel}}$, $\alpha_{H_{\perp}}$ and $\alpha_{H_{\parallel}}$ are the form factors associated to the respective fields, and they are proportional to the electric and magnetic polarizability of the perturbing object.

BEAD-PULL MEASUREMENTS

The bead-pull measurement technique exploits Slater’s perturbation theorem. In practice, a small perturbing object –referred to as bead– is inserted into the cavity suspended from a thin wire. The bead is then pulled along some path through the cavity while the resonance frequency is being monitored as a function of the position of the object.

Although the frequency shift can be measured directly, it may be hard to measure for small perturbations. For this

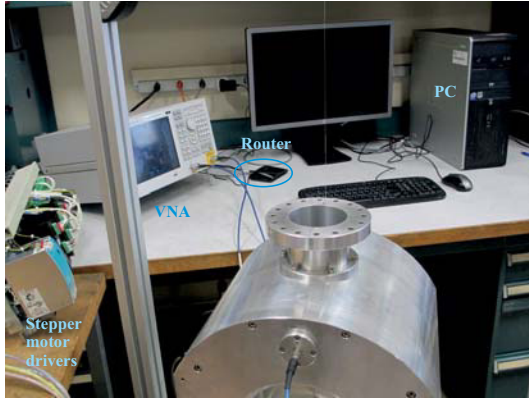


Figure 4: Bead-pull measurement setup.

reason, it is interesting to measure the frequency shift in an indirect way, by measuring the phase shift of a transmitted signal at the resonance frequency [10]. The relationship between frequency shift and phase shift is given by:

$$\frac{\Delta\omega}{\omega_0} = \frac{1}{2Q_L} \tan \Delta\phi$$

where Q_L is the loaded quality factor, and $\Delta\phi$ is the phase shift in radians of the S_{21} transmission parameter at ω_0 . Because of the non-linearity of the tan function, $\Delta\phi$ should be kept small enough (in practice, $\Delta\phi \lesssim 25^\circ$) so that errors in the $\Delta\phi$ measurement do not lead to considerable errors in the frequency shift estimation.

Figure 4 shows the bead-pull measurement setup used. The intelligence resides in the PC, which is running a software to control both the VNA and the drivers of the stepper motors. The three devices are interconnected by a router. The software to run the bead-pull measurements is encoded in LabVIEW [11], a graphical programming environment. Although hardly noticeable, a nylon wire is passing vertically through the beam-pipe. This wire is arranged in a closed loop and is driven by a motor connected to a pulley.

Two types of perturbing objects have been chosen (see Fig. 5). The sphere is chosen to measure the transverse components of the electromagnetic fields, both E_\perp and H_\perp . A metallic and a dielectric (stone) spheres of $\varnothing 5$ mm have been used. Unlike the non-directional sphere, the elongated shape of needle makes it more coupled to the longitudinal electric fields than to the transverse ones. Therefore, the needle is chosen as a perturbing object to measure the longitudinal components of the electric field, E_z . A 30-mm long needle with cylindrical shape ($\varnothing 1.2$ mm) has been used.



Figure 5: Perturbing objects used. From left to right: metallic sphere, dielectric sphere, cylindrical metallic needle.

TRANSVERSE COMPONENTS

Because of the non-directional geometry of the sphere, the perturbation effect becomes also non-directional as well, and the frequency shift of Eq. 1 becomes:

$$\frac{\Delta\omega}{\omega_0} = -\pi r^3 \varepsilon_0 \frac{|E_\perp|^2}{U} + \frac{1}{2} \pi r^3 \mu_0 \frac{|H_\perp|^2}{U}, \quad (2)$$

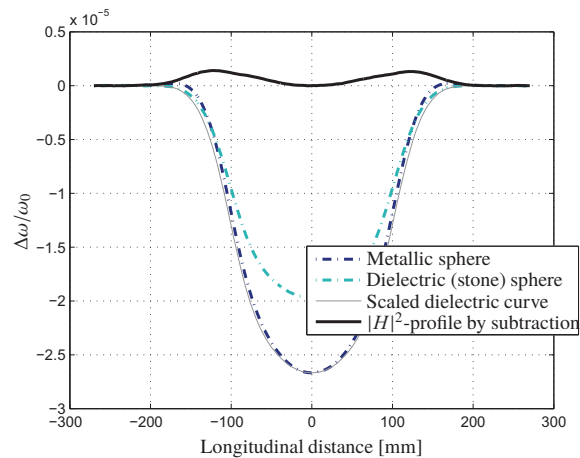
where r is the radius of the sphere. From Eq. 2, it is readily seen that a metallic sphere cannot distinguish between electric or magnetic fields separately, and the observed frequency shift will always be due to a combination of both E and H . In order to be able to separate both components, a dielectric (stone) sphere is used. It will only interact with the electric field in the following way:

$$\frac{\Delta\omega}{\omega_0} = -\pi r^3 \frac{\varepsilon_r - 1}{\varepsilon_r + 2} \varepsilon_0 \frac{|E_\perp|^2}{U}, \quad (3)$$

where ε_r is the relative permittivity of the material.

Figure 6 shows together the measurements coming from the metallic and the dielectric spheres, in the form of $\Delta\omega/\omega_0$ versus longitudinal distance. The averaged curves calculated over 30 measurements are shown. For the metallic sphere, $\Delta\omega/\omega_0 > 0$ at around $z = \pm 150$ mm, due to the contribution of H_y . No zero-crossing or positive frequency shift is found, though, in the dielectric measurements, which are proportional to the squared electric-field profile.

The magnetic field profile can be derived from these two measurements. On the one side, the magnetic field contribution is only contained in the measurements done with the metallic sphere (see Eq. 2). On the other side, the measurements with the dielectric sphere do only contain information about the electric field profile (see Eq. 3). Therefore, the magnetic field contribution is just hidden in the difference between the two measurements [12, 13].


 Figure 6: Averaged bead-pull measurements (over 30 measurements) using the metallic and dielectric spheres. The H_y profile is obtained by subtraction. The maximum standard deviation was about $1.35 \cdot 10^{-7}$ for the metallic sphere and $2.35 \cdot 10^{-7}$ for the dielectric one.

Before the subtraction, since the maximum central peak of E_x corresponds to a zero-crossing of H_y , the measurements with the dielectric bead will have to be scaled until the peak value reaches the peak value of the metallic-sphere measurements. The scaled measurements are represented in Fig. 6 as a continuous gray line. The squared magnetic-field profile is obtained by subtracting the scaled measurements of the dielectric sphere from the measurements of the metallic sphere. The subtracted trace is plotted as a black continuous line in the figure. The expected zero-passing in the middle of the trace can be clearly seen.

Knowing the absolute value of E_x and H_y is straightforward from Eqs. 2 and 3, provided the perturbing objects are calibrated. The calibration of the form factors of the different spheres has been done by doing on-axis measurements of the fundamental mode of the DQW cavity. Once the corresponding form factors are known, the absolute values of the measured electric and magnetic fields can be easily determined. A comparison between the measured fields and the simulated ones is shown in Fig. 7 and Fig. 8, where the

squared values of the normalized fields are plotted for E_x and H_y , respectively.

Firstly, the electric field is directly obtained from the dielectric-sphere measurements. Secondly, the magnetic field is derived from the metallic-sphere measurements. For the E_{\perp} value of Eq. 2, the derived E_x field plotted in Fig. 7 has been considered. A reasonably good matching between simulations and measurements can be observed, specially if considering that these values of Fig. 8 are one order of magnitude below the ones in Fig. 7.

LONGITUDINAL COMPONENTS

Ideally, a needle would only interact with the longitudinal field. However, in practice, due to the finite cross section of the needle and the strong transverse fields compared to the longitudinal ones, the effect of the transverse fields are also picked up in the measurements. The frequency shift in this particular case of a needle off-axis in the DQW is given by:

$$\frac{\Delta\omega}{\omega_0} = \alpha_{E_{n\perp}} \varepsilon_0 \frac{|E_{\perp}|^2}{U} + \alpha_{E_{n\parallel}} \varepsilon_0 \frac{|E_{\parallel}|^2}{U} + \alpha_{H_{n\perp}} \mu_0 \frac{|H_{\perp}|^2}{U}, \quad (4)$$

where the subscript n stands for “needle”. Since the objective is to measure E_z , the first and third addends can be seen as undesired measured components.

Figure 9 shows together the on-axis and off-axis (18 mm) measurements done with the needle, in the form of $\Delta\omega/\omega_0$ versus longitudinal distance. Again, the averaged curves calculated over 30 measurements are shown. The susceptibility of the needle to the transverse electric field is clearly demonstrated with the on-axis measurements. Due to the finite width of the needle ($\varnothing 1.2$ mm) and the strong transverse fields, a clear measurement of E_x is made on-axis. With the off-axis measurements, the contribution of the transverse E_x is also measured. Since the transverse fields

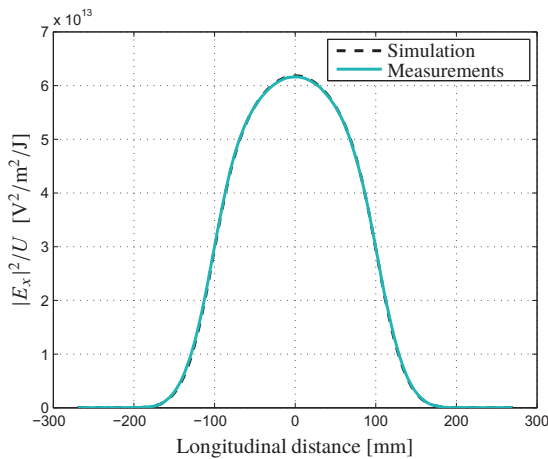


Figure 7: Simulation (HFSS) and measurements of the on-axis $|E_x|^2$, obtained after calibrating the spheres.

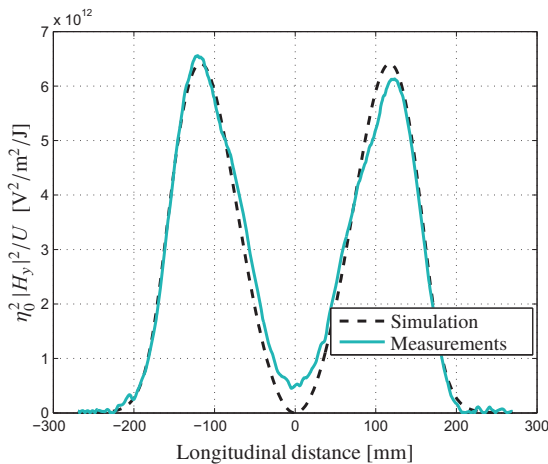


Figure 8: Simulation (HFSS) and measurements of the on-axis $\eta_0 |H_y|^2$, obtained after calibrating the spheres.

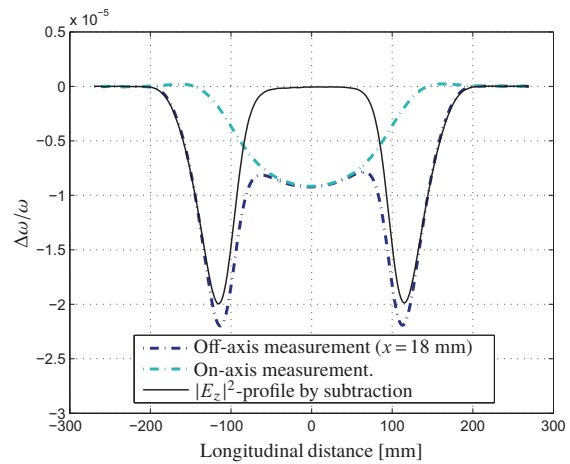


Figure 9: On-axis and off-axis (18 mm) averaged bead-pull measurements (over 30 measurements) using the needle. The E_z profile is obtained by subtraction. The maximum standard deviation were about $1.27 \cdot 10^{-7}$ for the on-axis measurements and $2.82 \cdot 10^{-7}$ for off-axis one.

on-axis have a negligible variation across the beam-pipe cross section, the off-axis measurements at the center of the cavity exactly overlap with the on-axis measurements. At around $z \approx \pm 100$ mm, symmetric peaks due to the longitudinal electric field can be noticed.

Getting the E_z profile is easy by taking into account the two following considerations. On the one hand, since there is no longitudinal field on-axis, the on-axis measurements only contains the information related to both transverse electric and magnetic fields, E_{\perp} and H_{\perp} , i.e., the first and third addends of Eq. 4. On the other hand, since the variation of E_{\perp} and H_{\perp} across the aperture can be considered negligible, the off-axis measurements contains the same information as the one in the on-axis measurements in addition to the information related to E_z , i.e., all the addends in Eq. 4. Therefore, the longitudinal electric field can be profiled just by subtracting the on-axis measurement from the off-axis one, as illustrated in Fig. 9 as a black continuous line.

Getting the absolute value of E_z is straightforward from the profiled E_z field depicted in Fig. 9, provided the longitudinal form factor of the needle, $\alpha_{E_{\parallel}}$, is known. To calibrate the needle, bead-pull measurements with the first higher-order mode of the DQW cavity have been done. This is a longitudinal mode with a very convenient field distribution for the needle calibration, since there is only longitudinal electric field on-axis.

Figure 10 shows a comparison between the measured fields and the simulated ones, where the squared values of the normalized fields are plotted. A good matching between simulation and measurements is found, specially considering that the values shown in Fig. 10 are two order of magnitude below those ones shown in Fig. 7 for E_x .

CONCLUSIONS

In this paper, RF measurements have been carried out on a full-scale aluminum prototype of the DQW crab cavity. The fundamental deflecting mode has been first analyzed by means of electromagnetic full-wave simulations. The different components of the electric and magnetic fields have been measured by means of the bead-pull technique. The transverse field components have been measured by means of spheres of different materials, in order to be able to distinguish between electric and magnetic fields. The longitudinal electric-field component has been measured by means of a metallic needle, having a higher susceptibility to longitudinal fields than to transverse ones. In both cases, both the profile and the absolute value have been determined and, the latter one, compared to the simulations as well. A good agreement between simulation and measurements has been found, confirming the reliability and accuracy of the measurements done.

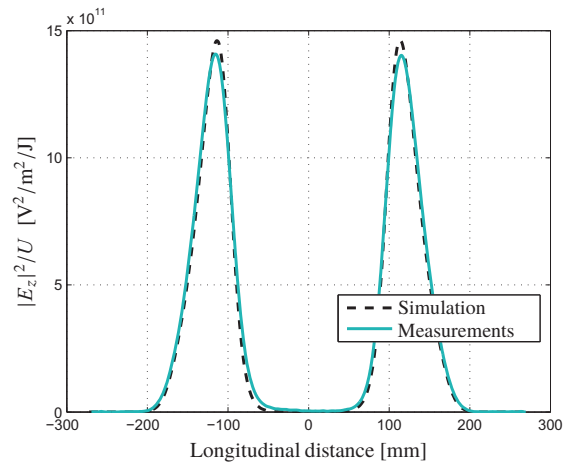


Figure 10: Simulation (HFSS) and measurements of the off-axis $|E_z|^2$, obtained after calibrating the needle.

REFERENCES

- [1] High Luminosity Large Hadron Collider HL-LHC, <http://hilumilhc.web.cern.ch>
- [2] P. Baudrenghien, K. Brodzinski, R. Calaga, O. Capatina, E. Jensen, A. Macpherson, E. Montesinos, and V. Parma, *Functional Specifications of the LHC Prototype Crab Cavity System*, CERN-ACC-NOTE-2013-003, February 2013.
- [3] I. Ben-Zvi *et al.*, “Quarter Wave Resonator”, Presented at *5th LHC CC Workshop*, Geneva, 2011.
- [4] T. Renaglia, “Cavity BNL Mock-Up Assembly”, EDMS note. <https://edms.cern.ch/document/1245841/0>
- [5] High Frequency Structure Simulator (HFSS), version 15.0, ANSYS Inc., Canonsburg, PA.
- [6] W. K. H. Panofsky, and W. A. Wenzel, *Some Considerations Concerning the Transverse Deflection of Charged Particles in Radio-Frequency Fields*, Review of Scientific Instruments, vol. 27, p. 967, 1956.
- [7] L. C. Maier, and J. C. Slater, *Field Strength Measurements in Resonant Cavities*, Journal of Applied Physics, vol. 3, no. 1, Jan. 1952.
- [8] Edward L. Ginzton, *Microwave Measurements*, New York: McGraw-Hill, 1957.
- [9] J. C. Slater, *Microwave Electronics*, New York: D. Van Nostrand Company, Inc., 1950.
- [10] F. Caspers and G. Dôme, Precise Perturbation Measurements of Resonant Cavities and Higher Order Mode Identification, in *Proc. of Conference on Precision Electromagnetic Measurements*, 4 pages, Delft, The Netherlands, 1984.
- [11] LabVIEW, version 2013. National Instruments, Austin, USA. <http://www.ni.com/labview>
- [12] B. Hall, *Designing the Four Rod Crab Cavity for the High-Luminosity LHC upgrade*, PhD dissertation, Sep. 2012.
- [13] D. Alesini, G. Di Pirro, L. Ficcadenti, A. Mostacci, L. Palumbo, J. Rosenzweig and C. Vaccarezza, *RF Deflector Design and Measurements for the Longitudinal and Transverse Phase Space Characterization at SPARC*, Nuclear Instruments and Methods in Physics Research A, vol. 568, pp. 488-502, 2006.